Analysis of deviatoric stress from nonhydrostatic pressure on a single crystal in a diamond anvil cell: The case of monoclinic aegirine, NaFeSi$_2$O$_6$

Robert T. Downs[a],*, A.K. Singh[b]

[a]Department of Geosciences, University of Arizona, Tucson AZ 85721-0077, USA
[b]Materials Science Division, National Aerospace Laboratories, Bangalore 560017, India

Abstract

A synthetic crystal of aegirine was compressed in a 4-pin diamond anvil cell with 4:1 methanol:ethanol + water mixture as a pressure-transmitting medium. The pressure was monitored using the shift of ruby R1–R2 lines. X-ray diffraction patterns were recorded at 17 pressures to 13.52 GPa using unfiltered Mo radiation. The pressure dependencies of the monoclinic cell parameters showed normal behavior to 11.55 GPa. The zero-pressure axial compressibilities were $\chi_a = 0.0029$, $\chi_b = 0.0031$, and $\chi_c = 0.0027 \, \text{GPa}^{-1}$. Fitting the third-order Birch–Murnaghan equation to the pressure–volume data yielded $K_0 = 117(1)$ GPa, $K_0' = 3.2(2)$, and $V_0 = 429.40(9) \, \text{Å}^3$. The average peak widths in all the runs to 11.55 GPa were ~0.08° in ω with small spread (standard deviation). At 12.62 and 13.52 GPa, a monoclinic unit cell did not fit well, as the standard deviations in cell parameters were 5–20 times the values obtained below 11.55 GPa. The cell parameters showed marked deviations from the trends exhibited by the data up to 11.55 GPa. Axial compressibilities over the range from 12.62 to 13.52 GPa were dramatically changed; $\chi_a = -0.0008$, $\chi_b = 0.0026$, and $\chi_c = 0.0006 \, \text{GPa}^{-1}$. The resulting discontinuity at 12.62 GPa in the pressure-volume plot was reminiscent of a pressure-induced phase transition. The average peak widths at these two pressures increased to ~0.24° with large spread. The analyses of the stress and strain tensors associated with the deviations in the cell parameter versus pressure plots at 12.62 GPa indicate the onset of nonhydrostatic stresses. At 13.52 GPa, just 2 GPa above the onset of nonhydrostatic strain, the magnitude of the nonhydrostatic stress was computed to be 1.2 GPa. Such a situation is likely to arise in high-pressure studies on single crystals. It is important to recognize in order to avoid incorrect interpretation of the data. The analysis presented in this article can be used in detecting the onset of nonhydrostatic stresses due either to freezing of the pressure-transmitting medium or to the sample bridging the anvils.

1. Introduction

Diamond anvil cells have been extensively used to apply pressure to single crystals and polycrystalline aggregates, and record the diffraction patterns. The pressure is rendered hydrostatic by containing the sample in a metal gasket filled with liquid or inert gas that acts as the pressure-transmitting medium (PTM). As the pressure is increased, the viscosity of the PTM increases. The stress state of the PTM (and, therefore, of the sample) deviates from hydrostatic soon after the pressure is stepped up but over time relaxes to a hydrostatic state. At high enough pressure, the viscosity becomes so large that the PTM begins to behave as a solid and the nonhydrostatic stresses do not relax in the time scale of the experiments. At this stage, the stresses in the PTM, and therefore in the sample, begins to depart from hydrostatic. The stress state becomes nonhydrostatic well before the PTM freezes if the sample begins to bridge the anvils. The magnitudes of the nonhydrostatic stress components are expected to be much larger in this case than those produced by the freezing of the PTM.

Treatment of diffraction data from polycrystalline solids under nonhydrostatic compression has received considerable attention. The nonhydrostatic stress state has been

*Corresponding author. Tel.: +1 520 626 8092; fax: +1 520 621 2672.
E-mail address: downs@geo.arizona.edu (R.T. Downs).

modeled [1] and the equations describing its effect on the peak positions and measured d-spacings have been derived [2–6]. Understanding in this field has reached a stage where it is possible to derive a measure of compressive strength of the sample material, the equation of state corresponding to hydrostatic compression, and the single-crystal elastic moduli from powder diffraction data taken under non-hydrostatic compression ([7] and references therein). Powder diffraction lines also tend to broaden significantly under nonhydrostatic stresses. Line width analysis gives information on the micro-strains and grain size [8,9]. In comparison, the behavior of single crystals under nonhy-drostatic compression has attracted attention of investiga-tors only recently. This is largely due to the fact that most investigators working with single crystals take care to limit the measurements to pressures below the freezing of PMT. Nonetheless, interesting observations have been made under nonhydrostatic pressures. The studies on single crystals of $CuGeO_3$ showed a sequence of phase transfor-mations under hydrostatic pressure that was different from the sequence observed under nonhydrostatic pressures [10]. The crystalline to amorphous transformations in a number of compounds shows strong dependence of transformation pressure on the presence of a nonhydrostatic stress component cf. [11–14]. Theoretical model calculations to examine phase transformations in silica subjected to a nonhydrostatic stress state suggest that α-quartz trans-forms to a stable phase with five-coordinated silicon—a coordination number that is not observed under hydro-static compression [15]. A fuller understanding of the behavior of solids under nonhydrostatic pressure may lead to the systematic synthesis of phases that are not formed under hydrostatic pressure.

There lies a region close to the freezing pressure where the nonhydrostatic stresses in the PTM produce subtle but measurable effects in the lattice parameters. Detection and treatment of such effects become important in the analysis of high precision data. In our recent high-pressure study on single crystals of aegirine, $NaFeSi_2O_6$ pyroxene, we observed anomalies in the pressure dependencies of unit cell parameters near the freezing pressure of the PTM (4:1 methanol: ethanol + water). The anomalies in the lattice parameters were accompanied by the broadening of the diffraction peaks. In this article, we record our observa-tions of effects produced by the nonhydrostatic stress state.

2. Experimental details

The diffraction experiments under pressure were con-ducted with unfiltered Mo radiation using a 4-pin diamond anvil cell (anvil culet size 600 μm) mounted on a Picker diffractometer. A 250-μm thick stainless steel gasket, pre-indented to 100 μm, with a 300-μm-diameter sample chamber filled with PTM (4:1 methanol: ethanol + water) was used to contain the sample. A small ruby chip placed close to the sample in the cell acted as the pressure marker. Pressures were determined from fitted positions of the R_1 and R_2 ruby

fluorescence spectra modeled as Lorentzian functions using the calibration of Mao et al. [16]. A single, euhedral synthetic crystal of aegirine from Redhammer et al. [17], run Nahp2, of size $\sim 115 \times 70 \times 50\ \mu m^3$ was selected on the basis of sharp diffraction spots and no evidence of twinning.

The peak positions of 25 strong reflections with $2\theta < 40^\circ$ from aegirine were determined by the 8-reflection centering technique of King and Finger [18] and used to refine the unit cell parameters. The centering algorithm was modified by including one more cycle of centering over each of three diffractometer angles as well as fitting the final ω-scan to the sum of the 2 Gaussian profiles that represent the Kα1 and Kα2 doublet. These two modifications resulted in a much better centering of the crystal, as evidenced by an order of magnitude reduction in the standard deviations of refined cell parameters. Measurements on aegirine were conducted at room pressure in air, and at 17 different pressures to 13.52 GPa. At room conditions a half-sphere of intensity data was collected for crystal structure determination to $2\theta \leqslant 60^\circ$, using ω scans of 1° width, step size of 0.025° and 3 s per step counting times. In addition, all accessible reflections at 9 different pressures were recorded under similar conditions except that each step was measured for 10 s. Finally, the pressure was raised to 14.6 GPa, but the peak widths became very large (greater than 0.33°) and diffraction data were not collected. The crystal was recovered from the cell and the diffraction peaks of a few strong reflections were reexamined.

3. Results and discussions

3.1. General considerations

The aegirine crystal was located at the center of the pressure chamber and was fastened to the diamond culet with a very small smear of Vaseline, as shown in Fig 1. The ruby chip was separated from the sample as well as the gasket edge. The face in contact with the diamond culet was (1 1 0). Fig 2 shows the R1–R2 doublet of the ruby-fluorescence spectrum recorded at ambient pressure and 13.52 GPa. The well-resolved peaks in the spectra indicate that the ruby chip did not bridge the anvils and experienced the pressure transmitted through only the PTM.

The crystal gave sharp diffraction peaks except at 12.62 GPa and above. Fig 3 shows the resolved Kα1 and Kα2 components of ($\bar{1}$ 0 1) peak at 8.63 and 13.52 GPa. The standard deviation, the square root of the variance of the Gaussian Kα1 component, was taken as the measure of the peak width. This approach of function fitting to the intensity-ω profile greatly enhanced the precision of the peak position and its width.

3.2. Compression behavior to 11.55 GPa

The unit cell parameters and volume of aegirine at different pressures are listed in Table 1, and shown in Figs. 4a and b, respectively. All the cell parameters and
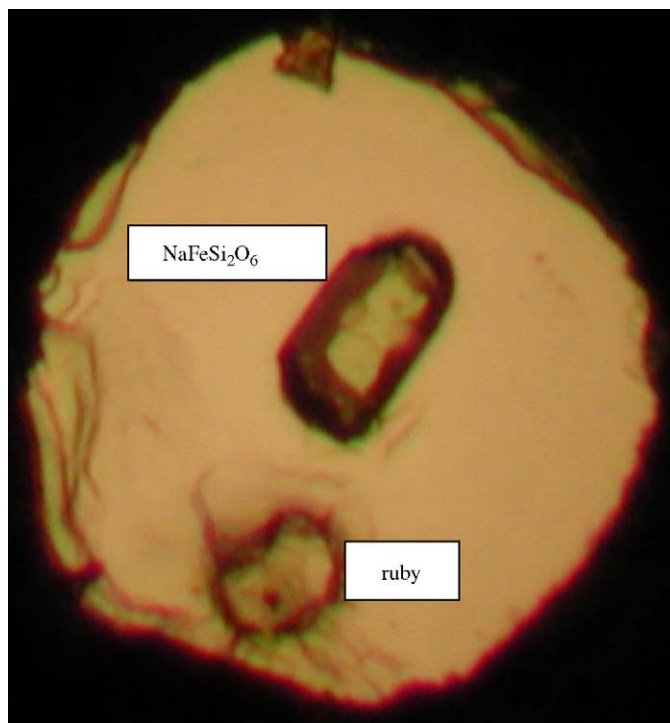
Fig. 1. The aegirine crystal remained at the center of the diamond anvil cell in the entire pressure range of the experiments. A ruby chip was placed away from the gasket edge.
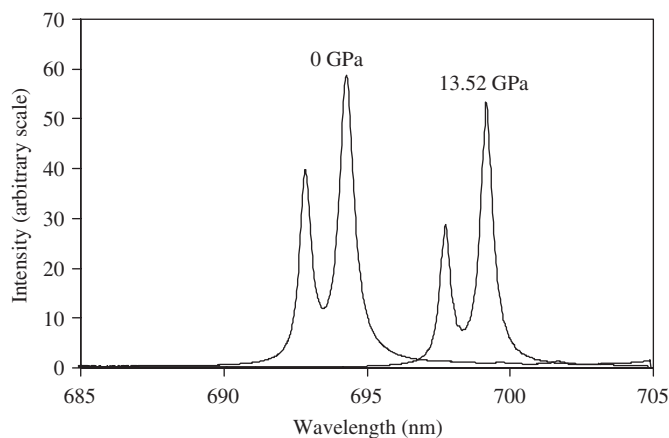

Fig. 2. The ruby R1 and R2 lines are well resolved and do not provide a hint about the stress conditions.

Fig. 3. A weighted sum of two Gaussian functions is adequate to separate the Kα1 and Kα2 intensity profiles.

volumes to 11.55 GPa show normal compression. The zero pressure axial compressibilities, $(1/x \ (\partial x/\partial P)_{P=0})$, were derived by fitting a second order polynomial to the cell-parameter-pressure data. The bulk modulus and its pressure derivative were derived by fitting a third-order Birch–Murnaghan equation to the pressure–volume data to 11.55 GPa. The present results have been compared with those derived from the single crystal elastic constants C_{ij} obtained from ultrasonic velocity measurements [19]. The elastic compliances S_{ij} were derived from C_{ij}. The elastic constants are referred to a standard Cartesian basis
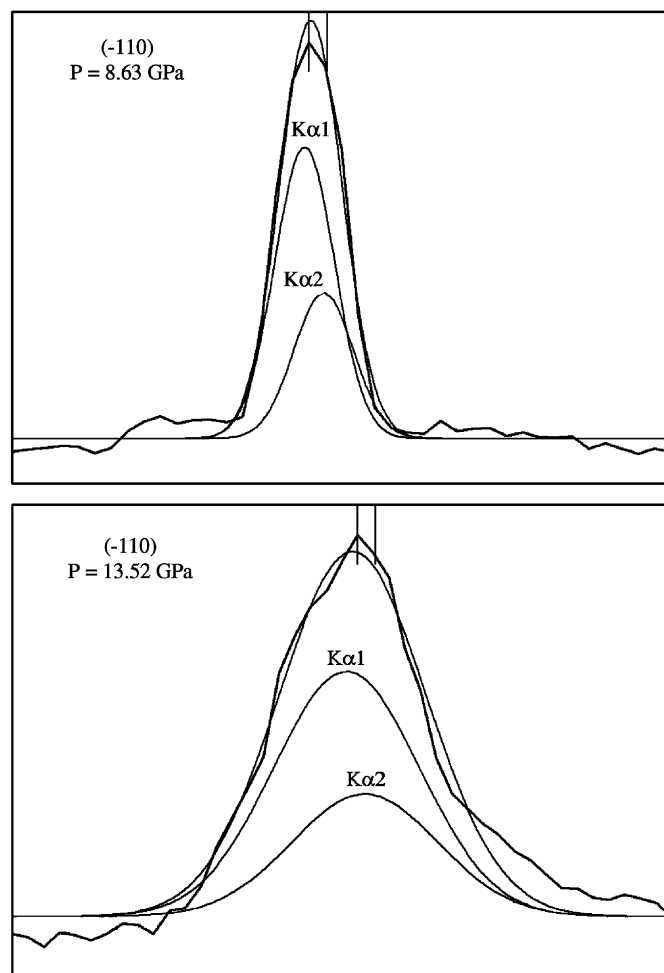
[20, p. 281] wherein the orthogonal set of axes are chosen such that the b-axis coincides with Ox_2 and the c-axis with Ox_3. The bulk modulus, relevant to single crystals under hydrostatic compression [20, p. 146], were calculated from the relation

$$(K_0)^{-1} = S_{11} + S_{22} + S_{33} + 2(S_{12} + S_{23} + S_{13}). \tag{1}$$

The axial compressibilities under hydrostatic pressure [20, p. 146] were calculated with the relations

$$\chi_a = (S_{11} + S_{12} + S_{13})\sin^2\beta, \tag{2a}$$

$$\chi_b = S_{12} + S_{22} + S_{23}, \tag{2b}$$

$$\chi_c = S_{13} + S_{23} + S_{33}. \tag{2c}$$

The results are given in Table 2. The bulk modulus obtained from the present measurement is $\sim$10% higher than the value obtained from the ultrasonic velocity measurements. The present values of the compressibilities along the a- and c-axis are in good agreement with the values calculated from Eqs. (2a) and (2c), respectively. However, the compressibility along the b-axis from the

Table 1
Cell parameters for Na-aegirine as a function of pressure

Run	P (GPa)	a	b	c	β	Vol (Å^3)
P0	0.0001	9.6539(2)	8.7928(2)	5.2935(2)	107.436(2)	428.69(2)
P1	0.56(3)	9.6406(3)	8.7825(5)	5.2871(2)	107.386(3)	427.20(3)
P2	1.20(3)	9.6221(4)	8.7644(4)	5.2778(2)	107.318(3)	424.91(3)
P3	1.78(3)	9.6067(3)	8.7501(4)	5.2698(2)	107.258(3)	423.03(2)
P4	2.62(3)	9.5858(4)	8.7307(5)	5.2585(2)	107.171(4)	420.47(3)
P5	3.35(3)	9.5667(4)	8.7128(5)	5.2484(2)	107.095(4)	418.14(3)
P7	5.47(3)	9.5148(3)	8.6568(3)	5.2188(3)	106.844(4)	411.42(3)
P7a	6.29(3)	9.4948(2)	8.6364(3)	5.2062(2)	106.757(3)	408.79(2)
P9	7.30(3)	9.4711(2)	8.6068(3)	5.1915(1)	106.633(2)	405.48(2)
P11	8.09(3)	9.4551(3)	8.5885(4)	5.1815(2)	106.551(3)	403.33(2)
P12	8.63(3)	9.4426(3)	8.5727(4)	5.1740(2)	106.482(3)	401.62(2)
P13	9.09(3)	9.4342(4)	8.5631(6)	5.1677(3)	106.439(4)	400.41(3)
P14	9.76(3)	9.4220(2)	8.5480(4)	5.1597(2)	106.371(3)	398.71(2)
P15	10.37(3)	9.4125(3)	8.5342(5)	5.1526(3)	106.314(4)	397.23(3)
P17	10.82(3)	9.4038(3)	8.5221(5)	5.1465(3)	106.256(4)	395.95(3)
P18	11.55(3)	9.3931(4)	8.5065(6)	5.1394(3)	106.187(4)	394.37(4)
P19	12.62(3)	9.3922(20)	8.4862(34)	5.1425(16)	106.073(22)	393.86(18)
P20	13.52(3)	9.3989(49)	8.4657(89)	5.1396(50)	106.057(54)	393.00(53)

Triclinic unit cell: P19: $a = 9.3827(9)$, $b = 8.4763(9)$, $c = 5.1405(5)$, $\alpha = 90.097(9)$, $\beta = 106.176(8)$, $\gamma = 90.177(8)$, $V = 392.634(65)$.
P20: $a = 9.3727(10)$, $b = 8.4361(10)$, $c = 5.1393(5)$, $\alpha = 90.050(9)$, $\beta = 106.150(7)$, $\gamma = 90.438(9)$, $V = 390.311(68)$.
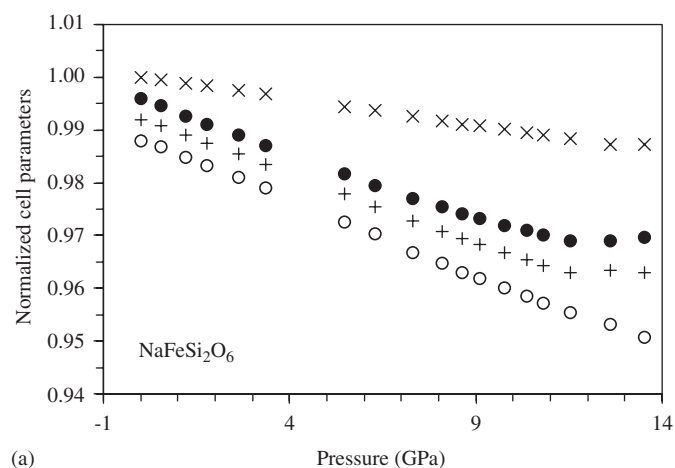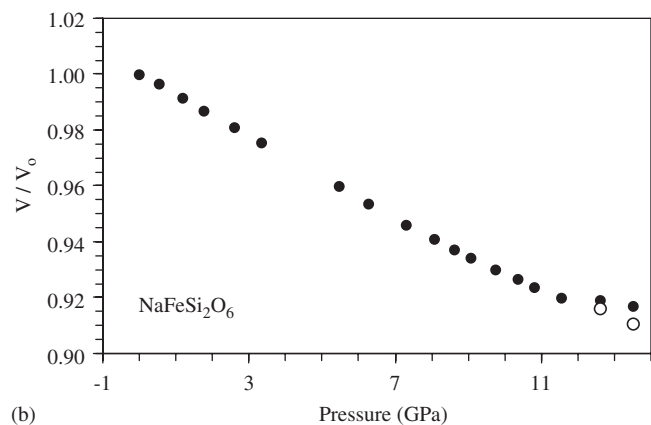
Fig. 4. (a) The normalized lattice parameters $(a/a_0)-0.004$, $(b/b_0)-0.012$, $(c/c_0)-0.008$, and (β/β_0) are shown by dots, circles, plus symbols, and crosses, respectively. The different data sets are shifted for clarity. (b) The dots and circles show the normalized unit cell volumes for the monoclinic and triclinic cells, respectively.

present measurement is $\sim$13% lower than the value calculated from Eq. (2c). It may be noted that the single-crystal elasticity data were obtained on naturally occurring aegirine, which is never found chemically pure, while the present measurements are on a synthetic aegirine crystal. The differences between the two sets of data shown in Table 2 are not significant in view of the fact that the elastic properties of pyroxenes are known to depend on composition [21].

In general, the strain can be modeled as an ellipsoid with orthogonal axes. One of the axes coincides with the two-fold symmetry axis of the monoclinic system, which in aegirine is the b-axis. The other two axes are constrained to lie in the a–c plane. The matrix associated with strain, S, between states $_1$ and $_0$ is computed from $S \cdot A_0 = A_1 - A_0$, where A represents the Direct to Cartesian transformation matrix [25]. The rotational components of strain are then removed by making the matrix symmetrical, $(S^t + S)/2$ [20]. The strain between $P_0 = 0$ and $P_1 = 11.55$ GPa was computed from the cell parameters listed in Table 1 using Ohashi's STRAIN software [22].

The analysis indicates that the compression of the unit cell in aegirine is anisotropic. The compressibilities along the three orthogonal axes of the ellipsoid are computed as $-0.00119(6)$, $-0.00282(6)$, and $-0.00312(5)$ GPa^{-1} with ratios 1:2.37:2.62, where the middle value represents the strain along the b-axis. These values are similar to those observed for other pyroxenes and summarized by [21]. Fig 5 shows the unit strain ellipsoid as viewed down the b-axis overlaying the structure of aegirine. In the crystal structure of aegirine, the anions form a distorted close packed array [23,24]. It has been shown that the most compressible direction is perpendicular to the closest

Table 2
The bulk modulus K_0, pressure derivative of the bulk modulus K'_0, and the axial compressibilities χ_a, χ_b, χ_c from this study are compared with those from ultrasonic velocity measurements

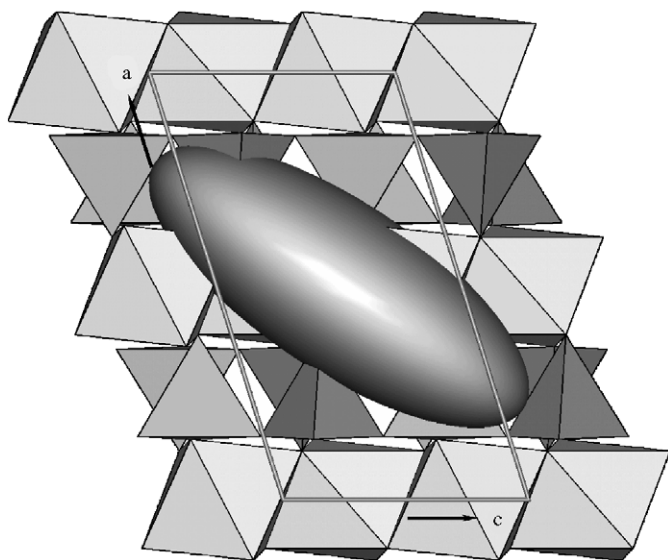|	K_0 (GPa)	K'_0	χ_a (GPa^{-1})	χ_b (GPa^{-1})	χ_c (GPa^{-1})
This study	117(1)	3.2(2)	0. 0029	0.0031	0.0027
Alexandrov et al. [19]	107	–	0.0029	0.0035	0.0026

Fig. 5. The orientation of the strain ellipsoid overlaying the projection of the structure down the b-axis.

Fig. 6. The dots show the average peak widths at different pressures. The error bars on either side of the mean values equal one standard deviation.

packing layer with the largest spacing, which coincides with direction $(\bar{1}\,0\,1)$ of the ideal structure [21]. The present results also show similar trends in the compressibilities.

3.3. Anomaly above 11.55 GPa

The data at the next two pressures, 12.62 and 13.52 GPa, indicate that the a- and c-parameters deviate significantly from the trends set by the data at lower pressures. The cell volumes at these two pressures also deviate appreciably. The errors of estimates in all the cell parameters increase by factors varying from ~5 to ~20. A triclinic unit cell fits the peak position data at these two pressures better, reducing the errors in the cell parameters to nearly double the errors for the monoclinic cell at lower pressures. Though the unit cell volume of the triclinic cell falls close to the extension of the curve drawn through the lower-pressure data points, the deviation is still clearly seen in Fig 4b. The discontinuity at 12.62 GPa in the pressure-volume plot resembles a phase transformation accompanied by a small volume change.

To understand the nature of the anomaly in the compression behavior at 12.62 GPa, the peak widths were examined. Fig 6a shows the average peak widths at diff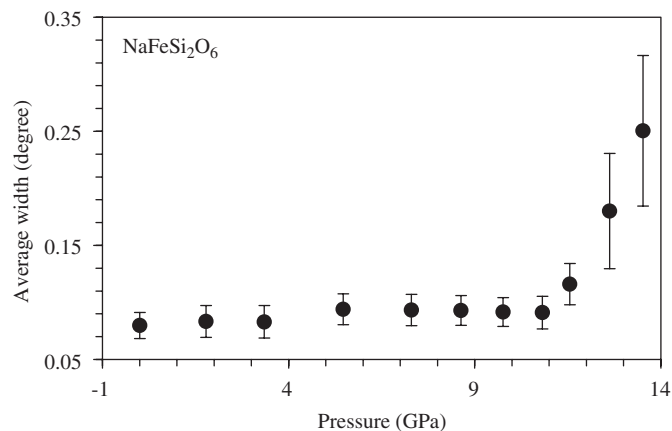erent pressures. It is 0.08° in ω with small spread at ambient pressures and remains practically unchanged up to 10.82 GPa. It increases noticeably at 11.55 GPa and becomes large at higher pressures, being 0.18° and 0.25°, respectively, at 12.62 and 13.52 GPa. The peak widths at 14.6 GPa became so large ($>0.33°$) that the standard procedure for crystal centering did not work. The average width at 14.6 GPa was in excess of 0.33°. The data at this pressure are not considered in this analysis, as the dataset was incomplete. These observations appear to suggest that the anomaly at 12.62 and 13.52 GPa in the compression behavior is accompanied by a concomitant increase in the line widths.

The strain associated with the anomaly at 13.52 GPa in the cell parameters was computed using Ohashi's STRAIN software [22] by considering two sets of cell parameters, one obtained by the extrapolation of the data below 11.55 to 13.52 GPa and the other obtained by fitting a monoclinic cell to the measured peak positions at 13.52 GPa (Table 1). The strain ellipsoid associated with nonhydrostatic stresses is much more isotropic in shape than the strain ellipsoid between 0 and 11.55 GPa, though the longest axes of both ellipsoids display the same orientations. The symmetric part of the strain tensor [25], referred to the standard orientation of the orthogonal set of axes (discussed earlier in the paper) is

$$\varepsilon_{ij} \times 10^3 = \begin{vmatrix} 4.15 & 0 & -0.75 \\ 0 & 1.19 & 0 \\ -0.75 & 0 & 5.20 \end{vmatrix}. \tag{3}$$

The stress causing this strain was computed using the relation

$$\sigma_i = c_{ij}\varepsilon_j. \tag{4}$$

The stresses, strains and elastic constants are in matrix notation with suffixes i and j running from 1 to 6 [20, p. 329]. The resulting stress tensor is

$$\sigma_{ij}(GPa) = \begin{vmatrix} 1.21 & 0 & 0.09 \\ 0 & 0.81 & 0 \\ 0.09 & 0 & 1.56 \end{vmatrix}. \tag{5}$$

The stresses in Eq. (5) are underestimated, as the pressure effects on C_{ij} are not considered. The anomalies in the cell parameters at 13.52 GPa are caused by the nonhydrostatic stress state given by Eq. (5). It is to be noted that these stresses appeared in the pressure range where the methanol-ethanol-water is known to freeze. It seems reasonable to assume that these stresses resulted from the freezing of the PTM. In that case, the PTM must develop enough strength soon after freezing to sustain nonhydrostatic stresses of the order of 1.20 GPa (the average of the diagonal terms of the σ_{ij} matrix in Eq. (5). A second factor that can give rise to nonhydrostatic stresses is the sample bridging the anvils. The freezing of the PTM is expected to cause a gradual increase of the nonhydrostatic stresses. The steep increase of peak widths above 11.55 GPa indicates a rapid increase in the magnitude of the nonhydrostatic stresses on the crystal. The peak widths of some of the strong reflections from the recovered crystal were of the same order as those observed at 14.6 GPa, and measured widths varied from $0.14°$ to $0.32°$. This indicates that the crystal suffered damage from the nonhydrostatic stresses.

4. Conclusions

The pressure dependencies of unit cell parameters show anomalies at 12.62 GPa and higher. The resulting anomaly in the pressure-volume plot can be wrongly interpreted as a phase transformation with a subtle volume anomaly. The large increase in peak widths above 11.55 GPa and analyses of the stresses and strains indicate that the phase-transformation-like situation, in fact, is an artifact due to the appearance of nonhydrostatic stresses. The analysis on the lines carried out in this article can be used to detect and investigate the onset of nonhydrostatic stresses in high-pressure X-ray diffraction studies on single crystals.

Aknowledgements

References

[1] A.L. Ruoff, Stress anisotropy in opposed anvil high-pressure cells, J. Appl. Phys. 46 (1975) 1389.

[2] A.K. Singh, The lattice strains in a specimen (cubic system) compressed nonhydrostatically in an opposed anvil device, J. Appl. Phys. 73 (1993) 4278; Erratum: 74, 5920.

[3] A.K. Singh, C. Balasingh, H.K. Mao, J. Shu, R.J. Hemley, Estimation of single crystal elastic moduli from polycrystalline X-ray diffraction at high pressure: applications to FeO and iron, Phys. Rev. Lett. 80 (1998) 2157.

[4] A.K. Singh, C. Balasingh, H.K. Mao, R.J. Hemley, J. Shu, Analysis of lattice strains measured under nonhydrostatic pressure, J. Appl. Phys. 83 (1998) 7567.

[5] T. Uchida, N. Funamori, T. Yagi, Lattice strains in crystals in uniaxial stress field, J. Appl. Phys. 80 (1996) 739.

[6] C.J. Howard, E.H. Kisi, Measurement of single crystal elastic constants by neutron diffraction, J. Appl. Crystallogr. 32 (1999) 624.

[7] A.K. Singh, X-ray diffraction from solids under nonhydrostatic compression–some recent studies, J. Phys. Chem. Solids 65 (2004) 1589.

[8] D.J. Weidner, Y. Wang, M.T. Vaughan, Geophys. Res. Lett. 21 (1994) 753.

[9] A.K. Singh, H.P. Liermann, S.K. Saxena, Strength of magnesium oxide under high pressure: evidence for the grain-size dependence, Solid State Commun. 132 (2004) 795.

[10] A. Jayaraman, S.R. Shieh, S.K. Sharma, L.C. Ming, S.Y. Wang, Pressure-induced phase transitions in $CuGeO_3$ from Raman spectroscopic studies, J. Raman Spectrosc. 32 (2001) 167.

[11] M.B. Kruger, R. Jeanloz, Memory glass—an amorphous material formed from $AlPO_4$, Science 249 (1990) 647.

[12] K.J. Kingma, C. Meade, R.J. Hemley, H.K. Mao, D.R. Veblen, Microstructural observations of α-quartz amorphization, Science 259 (1993) 666.

[13] S.M. Sharma, N. Garg, S.K. Sikka, High-pressure X-ray diffraction study of α-$AlPO_4$, Phys. Rev. B 62 (2000) 8824.

[14] J. Haines, J.M. Leger, F. Gorelli, M. Hanfland, Phys. Rev. Lett. 87 (2001) 155503.

[15] J. Badro, D.M. Teter, R.T. Downs, P. Gillet, R.J. Hemley, J.L. Barrat, Theoretical study of a five-coordinated silica polymorph, Phys. Rev. B 56 (1997) 5797.

[16] H.K. Mao, P.M. Bell, J.W. Shaner, D.J. Steinberg, Specific volume measurements of Cu, Mo, Pd, and Ag and the calibration of the ruby R1 fluorescence pressure gauge from 0.06 to 1 Mbar,, J. Appl. Phys. 49 (1978) 3276.

[17] G.J. Redhammer, G. Amthauer, W. Lottermoser, W. Treutmann, Synthesis and structural properties of clinopyroxenes of the hedenbergite $CaFeSi_2O_6$–aegirine $NaFeSi_2O_6$ solid-solution series, Eur. J. Mineral. 12 (2000) 105.

[18] H.E. King, L.W. Finger, Diffracted beam crystal centering and its application to high-pressure crystallography, J. Appl. Crystallogr. 12 (1979) 374.

[19] K.S. Alexandrov, T.V. Ryzhova, B.P. Belikov, Sov. Phys. Crystallogr. 8 (1964) 589.

[20] J.F. Nye, Physical Properties of Crystals–Their Representation by Tensors and Matrices, Clarendon Press, Oxford, England, 1985.

[21] M.J. Origlieri, R.T. Downs, R.M. Thompson, C.J.S. Pommier, M.B. Denton, G.E. Harlow, High-pressure crystal structure of kosmochlor, $NaCrSi_2O_6$, and systematics of anisotropic compression in pyroxenes, Am. Mineral. 88 (2003) 1025.

[22] R.M. Hazen, L.W. Finger, Comparative Crystal Chemistry, Wiley, New York, NY, 1982 231pp.

[23] R.M. Thompson, R.T. Downs, Model pyroxenes I: ideal pyroxene topologies, Am. Mineral. 88 (2003) 653.

[24] R.M. Thompson, R.T. Downs, Model pyroxenes II: structural variation as a function of tetrahedral rotation, Am. Mineral. 89 (2004) 614.

[25] R.M. Hazen, R.T. Downs, C.T. Prewitt, Principles of comparative crystal chemistry, in: R.M. Hazen, R.T. Downs (Eds.), Reviews in Mineralogy and Geochemistry, vol. 41, High-Temperature and High-Pressure Crystal Chemistry, Mineralogical Society of America, Washington DC, 2000.